RSC Advances

ROYAL SOCIETY OF CHEMISTRY

PAPER

View Article Online
View Journal | View Issue

Check for updates

Cite this: *RSC Adv.*, 2022, **12**, 13783

Preparation of a carbon fibre-reinforced carbon aerogel and its application as a high-temperature thermal insulator

Haiming Zhang,[a] Junzong Feng,[b] Liangjun Li,[b] Yonggang Jiang[b] and Jian Feng *[b]

Received 14th January 2022
Accepted 1st May 2022

DOI: 10.1039/d2ra00276k

rsc.li/rsc-advances

Carbon aerogels (CAs) have attracted attention in thermal insulation. However, the traditional sol–gel method for preparing them involves time-consuming solvent exchange and rigorous supercritical drying processes, and the obtained CAs are brittle and crumble easily. To address these problems, a carbon fibre-reinforced carbon aerogel (CF/CA) was prepared *via* combining a resorcinol–furfural (RF) gel containing a salt ($ZnCl_2$) with polyacrylonitrile (PAN) fiber felt. The CF/CA not only has low thermal conductivity (0.6904 W m^{-1} K^{-1}) even at an ultra-high temperature of 1800 °C in an argon atmosphere but also exhibits relatively high compressive strength (6.10 MPa, 10% ε) and a low density of 0.68 g cm^{-3}. The CF/CAs can be used as ultrahigh-temperature thermal insulators (under inert atmospheres or vacuum) in thermal protection systems such as space vehicles or industrial high temperature furnaces. Our novel strategy may lead to lower-cost and large scale industrial processes of CF/CAs.

1. Introduction

Among all aerogels to date,[1–9] carbon aerogels (CAs) have the highest thermal stability and can maintain their unique nanoporous structure even at temperatures as high as 2000 °C under inert atmospheres.[10–12] This high thermal stability of CAs, combined with excellent thermal insulation properties and low density, makes CAs promising candidates for ultrahigh temperature thermal insulation in thermal protection systems such as space vehicles or industrial high temperature furnaces.[13,14] However, CAs are brittle and fragile,[15] the mechanical properties of CAs can be improved by reinforcing them with fibres to form carbon fibre–carbon aerogel composites (CF/CAs).[16,17] The traditional sol–gel method for preparing CF/CAs involves solvent-exchange and supercritical-fluid drying processes,[18–22] organic waste liquids from the solvent-exchange process pollute the environment,[23] moreover, the supercritical-fluid drying process demands high-temperature and pressure conditions,[24,25] thereby increasing the safety risk and production costs.[26,27]

Many attempts have been made to prepare CAs by ambient drying.[28–31] For example, highly porous carbon was prepared using glucose as carbon precursor and eutectic of lithium chloride/zinc chloride as porogen, appearing as powder.[28] Hierarchical porous functional carbon was prepared by using ionic liquids as carbon precursor and eutectic mixture of LiCl/$ZnCl_2$ as salt template, the hierarchical porous carbon also appears as powder.[29] Mesoporous carbon aerogel was prepared by using calcium carbonate particles as salt template under ambient pressure drying, but the carbon precursor gel was subjected to solvent-exchange several times with petroleum ether.[30] Phenolic polymer-derived CA was prepared by direct polymerisation of reactive monomers phenol and formaldehyde under hypersaline conditions using $ZnCl_2$ salt, the phenol–formaldehyde–$ZnCl_2$ monolith was transformed into a foamy during the simultaneous carbonization and foaming processes, the foamy CA possess micron-sized macropores and cannot be used as a matrix for thermal-insulating CF/CA.[31] In practice, it is a challenge to prepare CF/CAs for thermal insulation by ambient pressure drying.[32–36]

In this study, CF/CA for thermal insulation was prepared by impregnating polyacrylonitrile (PAN) fibre felts with resorcinol (R)–furfural (F) sol containing salt ($ZnCl_2$), followed by ageing and pyrolysis. The RF sol containing salt was synthesized by direct polymerisation of R and F in methanol (MeOH) using $ZnCl_2$ as a salt template. Herein, salt template is acted as dehydration and porogens, a portion of salt combines with water molecules generated by the reaction of R and F to form $ZnCl_2 \cdot 4H_2O$ during the sol–gel process,[37] the RF gel with salt undergoes sufficient polycondensation reaction, thus enhancing the nano-skeleton strength of RF gel, the obtained CF/CA did not shrink largely during the carbonization process owing to its strengthness and the support of salt template. After carbonization, the salt template could be easily removed with water, the robust carbon skeleton can withstand the capillary force related to the surface tension of water during ambient

---

[a] *Institute of Applied Physics, Jiangxi Academy of Science, Nanchang 330096, China*

[b] *Science and Technology on Advanced Ceramic Fibres and Composites Laboratory, College of Aerospace Science and Engineering, National University of Defense Technology, Deya Road 109, Changsha, 410073, Hunan, China. E-mail: fengj@nudt.edu.cn*

pressure drying, thereby opening up abundant micropores and few mesopores in the CF/CA.[38–40] Abundant nanopores (pore size less than 69 nm) are efficient in reducing the total thermal conductivity by reducing the gaseous thermal conductivity,[41] moreover, the obtained CF/CA has significantly increased mechanical properties. Compared with the traditional sol–gel method for preparing CF/CAs,[41–44] this procedure eliminates the need for solvent-exchange and supercritical-fluid drying processes. To our knowledge, the preparation of CF/CAs *via* combining RF gel containing salt with PAN fiber felts has not been reported.

2. Experimental section

2.1 Materials

The reactive monomers, including R and F, $ZnCl_2$ and MeOH were supplied by Sinopharm Chemical Reagent Co. Ltd. Hexamethylenetetramine (HTM) was supplied by Tianjin Wind Boat Chemical Reagent Technology Co. Ltd. The polyacrylonitrile (PAN) fibre felt was purchased from Nantong Senyou Carbon Fibre Co. Ltd. The chemical reagents were obtained as analytical grade and used without any further purification.

2.2 Fabrication of carbon fibre-reinforced carbon aerogel

Carbon fiber reinforced carbon aerogel (CF/CA) was prepared by pyrolysis of resorcinol–furfural (RF) gel containing salt ($ZnCl_2$) reinforced by PAN fiber felts. Firstly, RF gel containing salt was synthesised *via* the sol–gel process using R and F as monomers, MeOH as solvent, HMT as catalyst, and $ZnCl_2$ as salt template. The flow chart for the preparation process is shown in Fig. 1. The F/R, HTM/R, MeOH/R and $ZnCl_2$/R molar ratios were 2, 0.024, 12 and 1.0, respectively. After thoroughly blending the chemical reagents, RF sol with salt was obtained. Then, PAN/RF sol with salt was prepared by impregnating PAN fibre felt (apparent density: 0.12 g cm^{-3}) with RF sol with salt under vacuum. The PAN/RF sol with salt was sealed with a plastic film and immersed in a 50 °C water bath pot for 24 h. RF sol with salt undergoes sufficient chemical cross-linking reaction during aging treatment and transforms into a RF gel with salt, which exhibits high mechanical strength. The PAN/RF gel with salt was carbonized directly at 650 °C for 2 h under nitrogen flow (200 ml min^{-1}) with a heating rate of 2.5 °C min^{-1}. The obtained salt-containing CF/CA was soaked in deionised water to remove salt template and dried in ambient pressure, then, the CF/CA (Fig. 2a) was obtained. CA (Fig. 2b) was also prepared by pyrolysing RF gel with salt under the same condition of preparing CF/CA.

2.3 Characterizations

The linear shrinkage rate (L_{shri}) of the samples was calculated from the dimension of the samples before and after carbonization according to eqn (1). D_{before} and D_{after} refer to the radial diameter of the samples before and after carbonization process.

$$L_{shri}\ (\%) = \frac{D_{before} - D_{after}}{D_{before}} \times 100\% \tag{1}$$

The bulk densities of the CA or CF/CA were obtained by measuring the mass and corresponding volume. The weight change of the PAN/RF gel with salt during carbonization under a flowing argon atmosphere was investigated by a NETZSCH STA 449F3 thermogravimetric (TG) analyzer, the heating rate was 10 °C min^{-1}, and the heating temperature range was from room temperature up to 1500 °C, the thermal stability of the CA in air atmosphere was investigated by TG (NETZSCH STA 449F3 thermogravimetric analyzer). The pore properties of the CA and CF/CA were determined by a 3H-2000PM2 apparatus from BeiShiDe Instrument, the specific surface area of the samples was calculated by applying Brunauer–Emmett–Teller (BET) method. The Barrett–Joyner–Halenda (BJH) model was applied to calculate the total pore volume from the adsorption–desorption isotherms. Pore size distribution curves were calculated by NLDFT method from the desorption branches. Horvath–Kawazoe (H–K) theory also was applied to derive pore size distribution. The microstructure of the samples were investigated by A Hitachi S-4800 scanning electron microscopy (Japan) after being coated with a thin gold layer. The microstructure surface of the CF/CA and CA were investigated using

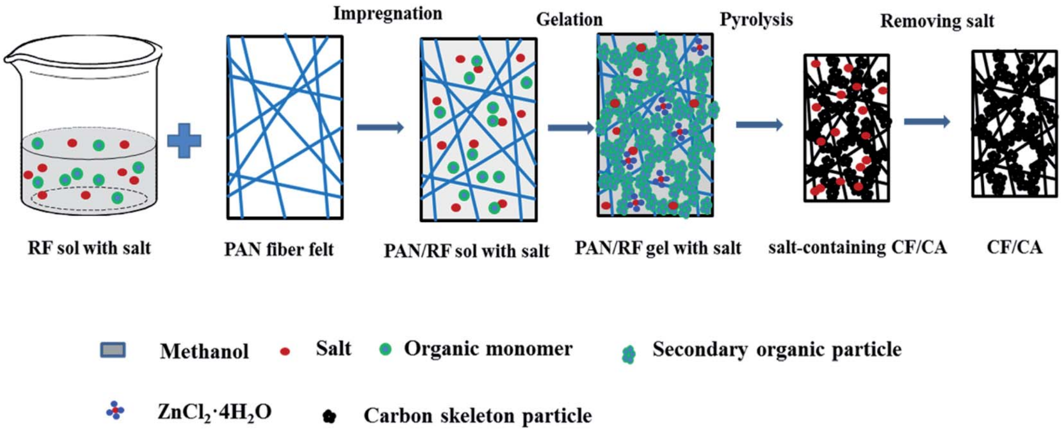

Fig. 1 Flow chart for the preparation of carbon fibre-reinforced carbon aerogel (CF/CA).

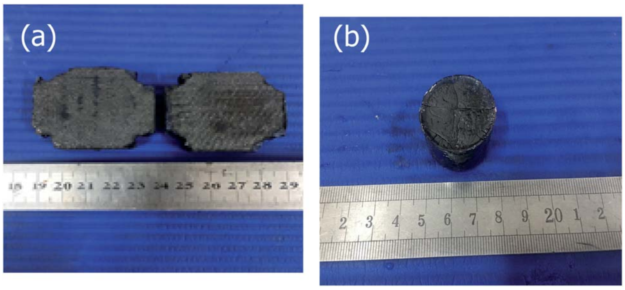

Fig. 2 The photographs of CF/CA (a) and CA (b).

Tecnai G2 F20 S-TWIN field emission transmission electron microscope (TEM) system, the samples were ground and dispersed with ethanol before placing it on a copper grid and analyzing them at 300 kV. X-ray photoemission spectroscopy (XPS; ESCALAB 250Xi) and CHN element analysis were applied to determine element percentages of the CF/CA. The crystal phase structure of the CAs prepared at different temperatures were characterized by a D8 Advance X-ray diffraction (XRD) apparatus using Cu K_α radiation with a Ni filter. Raman spectroscopy (Renishaw RM2000) was used to examine the graphitization degree of the CAs prepared at different temperature. The compression strength of the CF/CA was tested by universal testing machine (WDW model 100) with sample dimensions of 15 × 15 × 15 mm. The CF/CA was cut into cube-shape with diameters of 10 mm and thicknesses of approximately 2.0 mm, the thermal diffusivity (α) in the through-plane direction of the samples was determined by laser flash method using a Netzsch LFA 427 apparatus in argon atmosphere, the thermal conductivity (λ) was obtained according to eqn (2).[45]

$$\lambda = \alpha(T)\rho c_{\mathrm{p}}(T) \tag{2}$$

T is the temperature of measurement, ρ refers to the density of the CF/CA, $c_{\mathrm{p}}(T)$ is a known literature value of specific heat capacity.[46]

3. Results and discussion

3.1 Thermogravimetric analysis

The weight change of the PAN/RF gel with salt during heat treatment process was investigated by TG-DSC under a flowing argon atmosphere, the heating rate was 10 °C min^{-1}, and the heating temperature range was from room temperature up to 1500 °C. The weight loss curve during heat treatment process is shown in Fig. 3. The weight change is 62% in the temperature range from room temperature up to 1500 °C. Firstly, it can be seen that a weight loss (11%) takes place in the range from room temperature to 160 °C, which is due to the evaporation of methanol solvent as well as the evaporation of water molecules generated from the reaction of resorcinol and furfural. Secondly, a larger weight loss (35%) is observed in the temperature range from 160 to 600 °C, which is attributed to the release of some gas molecules in the pyrolysis process of PAN/RF gel with salt. Finally, a fairly small weight loss (only 16%) is observed in the temperature range from 600 °C to 1500 °C, which is mainly attributed to the continuous pyrolysis carbonization of organic group and the evaporation of some zinc chloride. In addition, DSC curve shows one exothermic peak in the two temperature intervals of 80–120 °C and 1300–1400 °C, respectively.

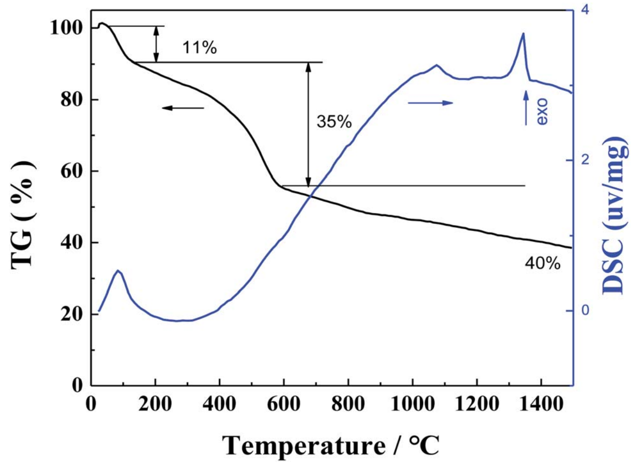

Fig. 3 TG-DSC curves of the PAN/RF gel with salt in argon atmosphere.

In order to study the thermal stability of the CA in air atmosphere, the weight change of the CA during heat treatment process was investigated by TG-DSC under a flowing air atmosphere, the heating rate is 5 °C min^{-1}, and the heating temperature range is from room temperature to 1200 °C. The TG-DSC curves of CA in air atmosphere is shown in Fig. 4. Firstly, it can be seen that a weight loss (8%) takes place in the range from room temperature to 100 °C, which is due to the evaporation of residual water in the CA. When the heating temperature increases to 450 °C, the CA begins to be oxidized in air atmosphere, a significantly larger weight loss (92%) is observed for CA in the range from 450 to 620 °C. In addition, DSC curve shows one endothermic peak in the temperature interval of 450–620 °C.

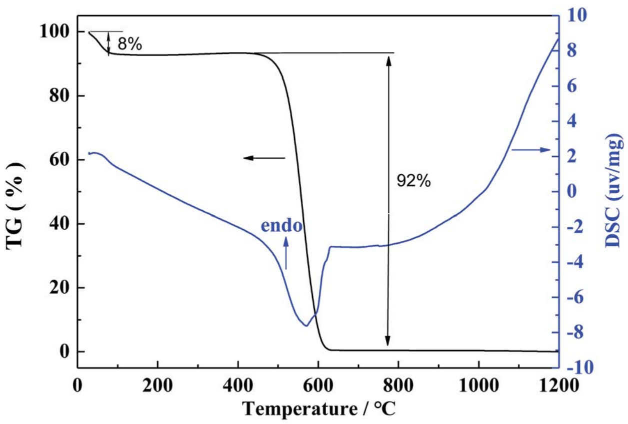

Fig. 4 TG-DSC curves of CA in air atmosphere.

3.2 Porous structure characterization

The N_2 adsorption–desorption isotherm curve and pore size distribution curves in Fig. 5 are used to analyze the porous structure of CA without salt, CA and CF/CA. According to classification of IUPAC, both the isotherm curves (Fig. 5a and b) are similar and exhibit a typical feature of type-I isotherm, which infers that microporous adsorption potential energy is very large and microporous specific surface area is much larger than external specific surface area. A sharp rise of the N_2 adsorption–desorption isotherm curves at low relative pressure scope ($P/P_0 \leqq 0.01$) infers the presence of abundant microporous, which is in agreement with the nanoporous structure parameters of CA and CF/CA shown in Table 1. From the micropore size distribution curves depending on NL-DFT model (Fig. 5c), it can be seen that the modal peaks occur at a pore size diameter of 0.8 nm and the pore sizes are focused in a range of 0.5–1.8 nm

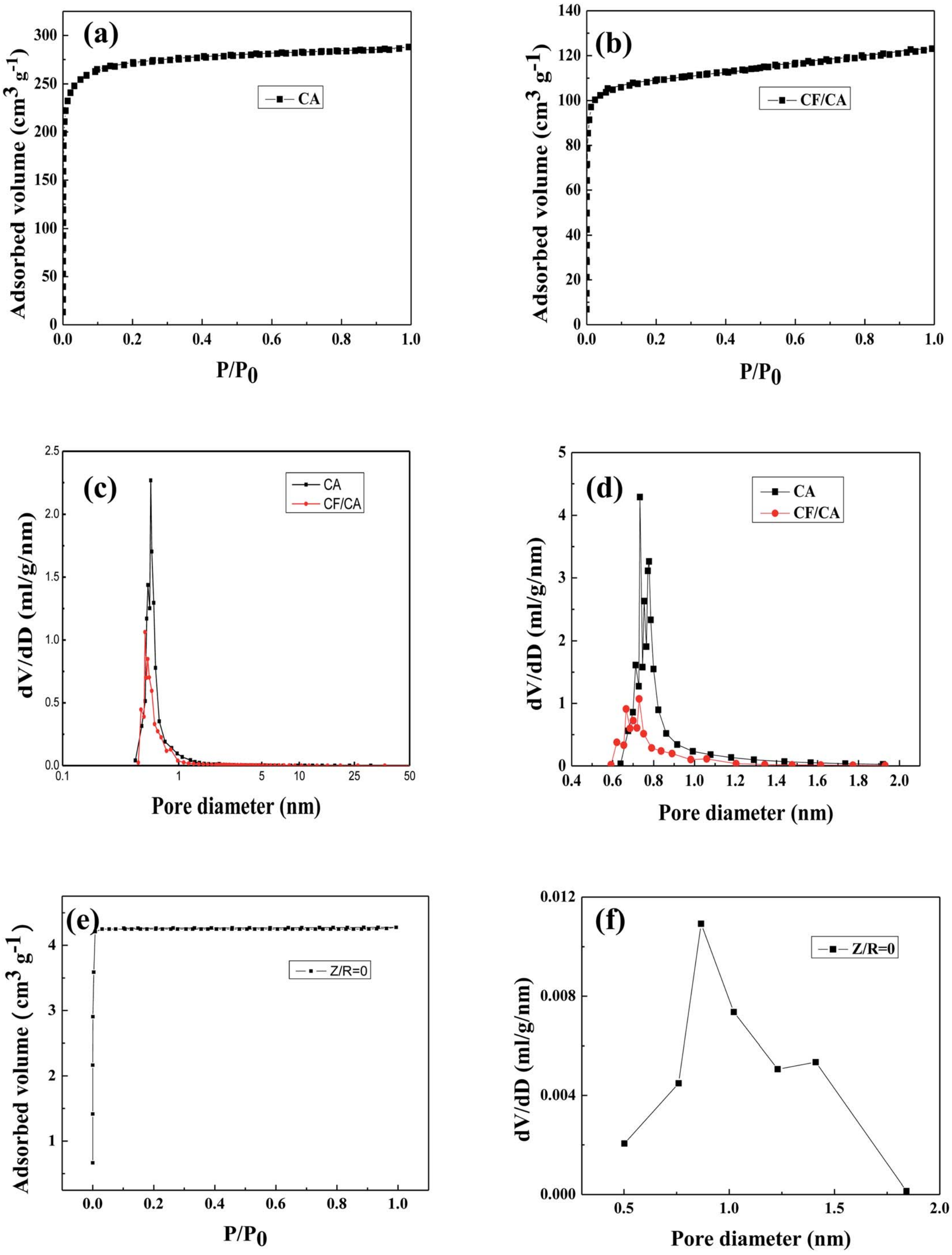

Fig. 5 The nitrogen adsorption isotherms (a and b), NL-DFT pore size distribution (c) and H–K pore size distribution curves (d) of CA and CF/CA, the nitrogen adsorption isotherms (e) and H–K size distribution curves (f) of CA without salt.

Table 1 BET surface area and nanoporous structure parameters of CA without salt, CA, and CF/CA

Sample	S_{BET} (m^2 g^{-1})	S_{micro} (m^2 g^{-1})	S_{ext} (m^2 g^{-1})	V_{pore} (cm^3 g^{-1})	D_{pore} (nm)
CA without salt	15.69	15.69	0	0.006	1.68
CA	818.98	815.44	3.54	0.327	1.60
CF/CA	425.66	405.74	19.92	0.190	1.78

for the CA and CF/CA. Fig. 5d shows the pore size distribution curves of CA and CF/CA derived from the H–K method, the pore sizes are focused in a range of 0.6–1.6 nm for the CAs and CF/CA, the modal peak value appears at 0.7 nm. Fig. 5e shows the N_2 adsorption–desorption isotherms curves of CA without salt, the isotherm curves exhibit IUPAC type-I curves, an abrupt but small rise of adsorbed volume at a very low relative pressure (P/P_0 < 0.1), indicating the presence of a little microporous. Fig. 5f shows the pore size distribution curves of CA without salt derived from the H–K method, the pore sizes are focused in a range of 0.5–1.8 nm and the modal peak value occurs at about 0.8 nm for the CA without salt.

Table 1 lists the BET surface area and nanoporous structure parameters of CA without salt, CA, and CF/CA. The BET specific surface area of CA was 818.98 m^2 g^{-1}, the BET surface area is mainly composed of microporous specific surface area. $ZnCl_2$ salt plays a key role in the microporous formation of CA, serving as dehydration agent and porogen. A portion of the salt combines with water molecules generated by the reaction of R and F to form $ZnCl_2 \cdot 4H_2O$ crystal during the sol–gel process. A part $ZnCl_2$ salt is embedded in the RF gel skeleton, the other part of $ZnCl_2$ salt and $ZnCl_2 \cdot 4H_2O$ crystal are dispersed in the nanopores of the RF gel. After pyrolysis, removing salt with water and drying at ambient pressure, thereby opening up abundant microporous and few mesoporous in CA and CF/CA. The nanopore formation mechanism *via* salt template is shown in Fig. 6. The total pore volume and BET specific surface area of CA are much higher than that of CF/CA, which is mainly attributed to the introduction of carbon fibres, carbon fibres possess negligible pore volume and specific surface area coMPared with CA. The mean pore sizes of CA and CF/CA are similar. The external specific surface of CF/CA is slightly bigger than that of CA. In contrast, the synthesis of CA without salt only result in dense structures, the specific surface area of CA without salt was 15.69 m^2 g^{-1}, which was completely composed of microporous specific surface area, and its pore volume is 0.006 cm^3 g^{-1}. Thus, the absent of mesoporous or macroporous structure in CA without salt is determined by the intrinsic property of resorcinol–furfural (RF) gel.

3.3 SEM and TEM observation

The SEM images of CF/CA and CA are shown in Fig. 7(a–d). Fig. 7a shows that an important feature of CF/CA is the tightly integration between carbon fibre reinforcement and matrix, the matrix fill in the space among carbon fibres, separating carbon fibres from one another, and enveloping them. Fig. 7b shows that there are not any micron macropores and obvious cracks in the matrix of CF/CA, the CA matrix has uneven surface. The uneven surface of the CA was consisted of carbon nanoflakes, the carbon nanoflakes size are focused in a range of 20–30 nm, which were interconnected to form a 3D nanoporous network structure, as shown in the high magnification SEM (Fig. 7c and d). The TEM micrographs of the CF/CA and CA are shown in Fig. 7d and e, there was no apparent difference in the micro-texture between the CF/CA and CA, they have a similar three-dimension nanoporous network structure, the solid phase is composed of interconnected particles with diameter less than 5 nm, the nanopore size is smaller than 5 nm.

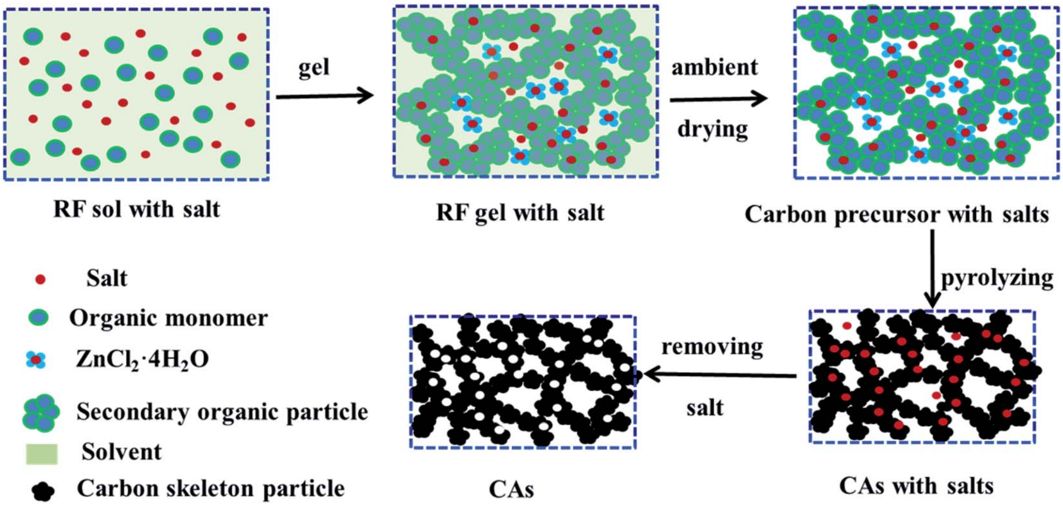

Fig. 6 Nanopore formation mechanism of preparing CAs *via* salt template.

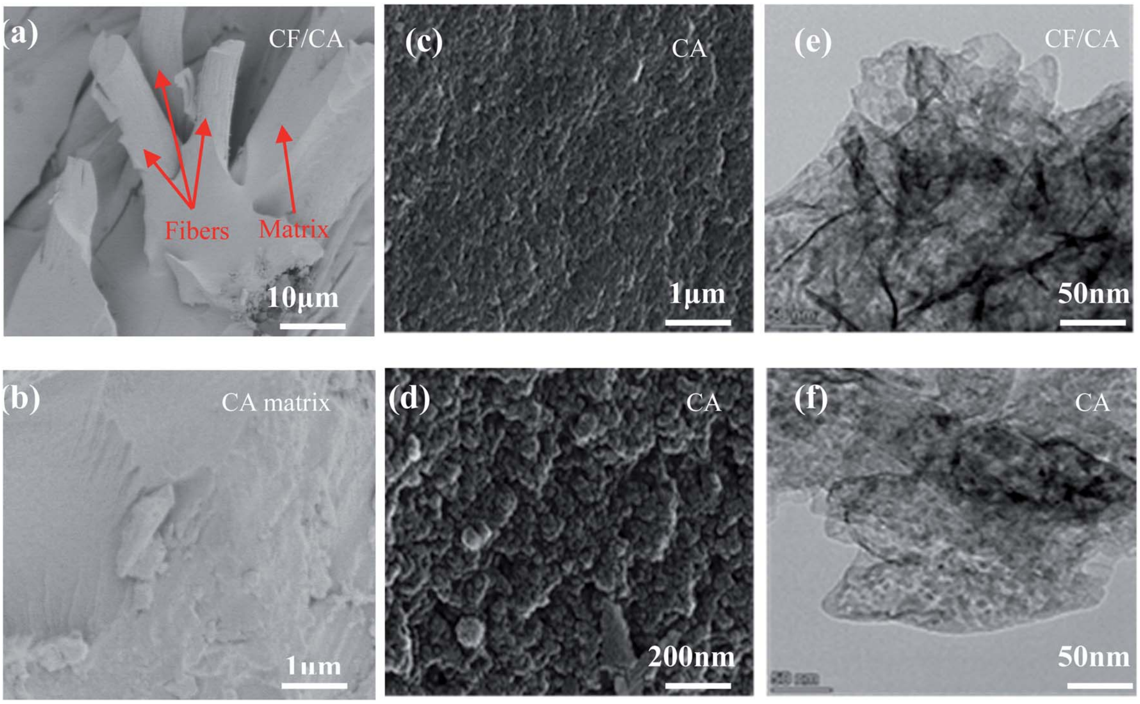

Fig. 7 (a–d) SEM and (e and f) TEM images of CA and CF/CA.

3.4 Optical images, XRD patterns, and Raman spectra of the CAs

The optical images of the CAs prepared at different temperatures are shown in Fig. 8. It can be seen that the surface of monolithic CAs prepared at different temperatures is similar and smooth, there are no micron-sized macropores.

X-ray diffraction patterns of CAs prepared at different carbonization temperatures are shown in Fig. 9. There are not any sharp peaks, indicating that the CAs are basically amorphous. The two broad peaks in the diffraction patterns are corresponded to slightly disordered graphitic carbon at about $2\theta = 23°$and $2\theta = 44°$.

The Raman spectra of CAs prepared at different carbonization temperatures is shown in Fig. 10. Two typical peaks at around 1370 cm^{-1} and 1600 cm^{-1} are observed, matching with the disordered structure (D-band) and graphitic structure (G-band) of CAs, respectively. With the increase of temperature, the I_D/I_G values (1.026, 1.024, 1.027 and 1.022) for CA$_S$ prepared at different carbonization temperatures (650 °C, 750 °C, 850 °C, and 950 °C, respectively) hardly changed, indicating that the graphitization degree of CAs did not change in the carbonization temperature range from 650 to 950 °C.

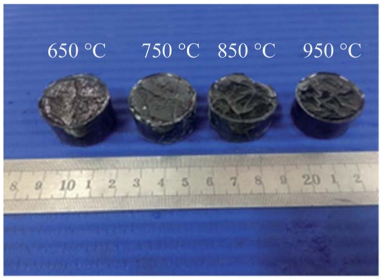

Fig. 8 Optical images of the CAs at different carbonization temperatures for 2 h.

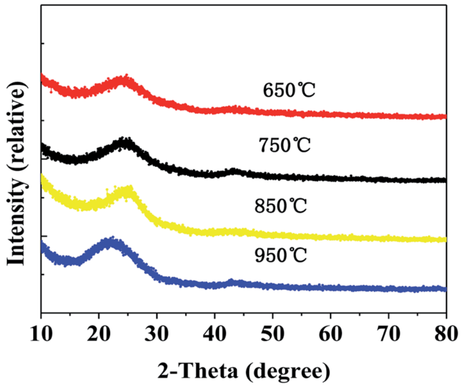

Fig. 9 XRD patterns of the CAs at different carbonization temperatures for 2 h.

3.5 Compositional anlysis

Elemental percentages of the CF/CA was analysed by XPS. Table 2 shows the elemental percentages of the CF/CA, the percentages of element such as carbon, nitrogen, oxygen, chlorine and zinc remaining in the CF/CA are 92.32%, 1.1%, 6.12%, 0.23%, and 0.23%, respectively. Because the residual salt could be easily removed with water, the residual salt content remaining

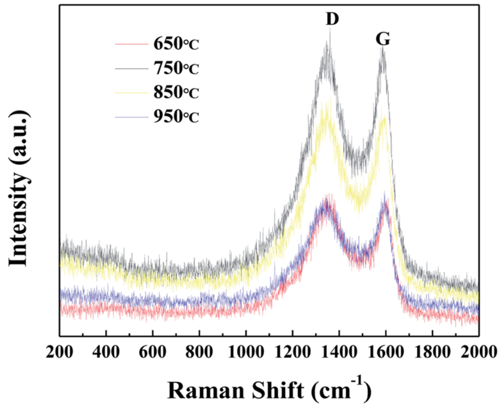

Fig. 10 Raman spectra of the CAs at different carbonization temperatures for 2 h.

Table 2 XPS elemental percentages of the CF/CA

Element	C	N	O	Cl	Zn
Content (at%)	92.32	1.1	6.12	0.23	0.23

Table 3 CHN elemental percentages of the CF/CA

Element	C	H	N	O
Content (at%)	87.54	2.66	1.05	8.75

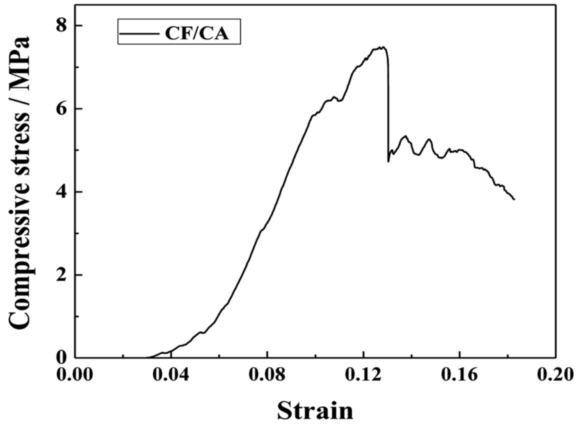

Fig. 11 Compression stress *versus* strain curve of the CF/CA.

Table 4 Shrinkage and density of CA and CF/CA

Material	Linear shrinkage during carbonization (%)	Density (g cm^{-3})
CA	25.14	0.71
CF/CA	12.16	0.62

in the CF/CA is extremely low, and they have almost no effect on the structure and properties of the CF/CA.

Table 3 shows the percentage of elements of carbon, hydrogen and nitrogen remaining in the CF/CA. According to CHN element analysis, C, H, N, and O element percentages of the CF/CA are 87.54%, 2.66%, 1.05%, and 8.75%, respectively.

3.6 Compressive strength of the CF/CA

Fig. 11 shows the compression stress *versus* strain curve of the CF/CA. It can be seen that, for the CF/CA, the compressive stress *versus* strain curves show elastic deformation at the initial stage. The compression stress increases exponentially as the strain increases before the specimen is fractured, the compression stress is 6.10 MPa when the strain is 0.1. When the compressive stress of the CF/CA increases to the highest point, the CF/CA begins to fracture abruptly, then the compressive stress of the CF/CA decreases as the strain increases gradually, indicative of toughness fracture behavior of the CF/CA.[47] The brittleness and fragility of CAs could be improved by reinforcing the CF/CA with PAN fibre felts.

3.7 Thermal conductivities of the CF/CA

Table 4 shows the shrinkage and density of the CA and CF/CA, the linear shrinkage of CA is much higher than CF/CA during the carbonization process, the densities of the CA and CF/CA are 0.71 g cm^{-3} and 0.62 g cm^{-3}, respectively.

The specific heat is mainly related to the composition of the material, both CF/CA and CA are mainly composed of carbon. Therefore, the same specific heat is used for both CF/CA and CA when calculating thermal conductivity, the specific heat value of CF/CA was a known literature value of specific heat capacity.[46] Fig. 12 shows that the specific heat values of CF/CA at different temperatures up to 2000 °C under argon, the specific heat values of CF/CA at the different measurement temperature (600 °C, 900 °C, 1200 °C, 1500 °C and 1800 °C) are 1.75 J g^{-1} K^{-1}, 1.98 J g^{-1} K^{-1}, 2.05 J g^{-1} K^{-1}, 2.10 J g^{-1} K^{-1}, 2.12 J g^{-1} K^{-1}, respectively.

Fig. 13 shows the thermal diffusivities of the CF/CA at the measurement temperatures ranging from 600 °C to 1800 °C in

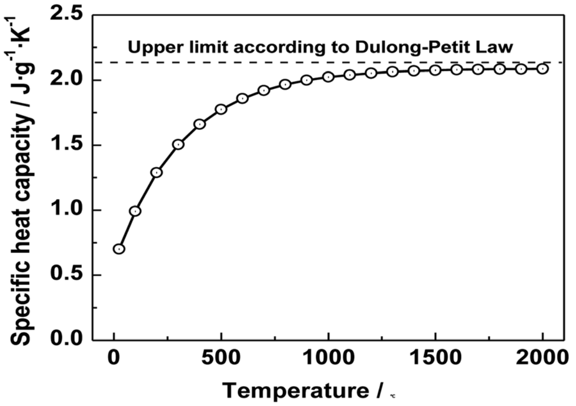

Fig. 12 Specific heat capacity used for calculating thermal conductivity.

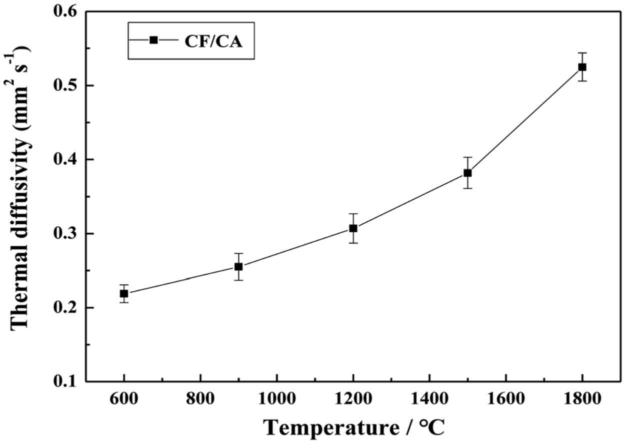

Fig. 13 Thermal diffusivities of the CF/CA at different measurement temperature in argon atmosphere. The error bars indicate the standard error of twenty results of five measurement temperatures, with four flash pulses for each measurement temperature.

argon atmosphere, the thermal diffusivities increase with increasing the temperature. The thermal diffusivities of CF/CA at the different measurement temperature (600 °C, 900 °C, 1200 °C, 1500 °C and 1800 °C) are 0.219 mm^2 s^{-1}, 0.255 mm^2 s^{-1}, 0.307 mm^2 s^{-1}, 0.382 mm^2 s^{-1}, 0.525 mm^2 s^{-1}, respectively.

The thermal conductivity was obtained according to eqn (2) from the thermal diffusivity, the specific heat capacity and the density. Fig. 14 shows the thermal conductivities of the CF/CA at the temperatures ranging from 600 °C to 1800 °C in argon atmosphere. The thermal conductivities of the CF/CA increase gradually from 0.2381 W m^{-1} K^{-1} to 0.6904 W m^{-1} K^{-1} in the temperature interval of 600–1800 °C. Under the ultrahigh temperature 1800 °C and argon atmosphere, the thermal conductivity of the CF/CA (0.6904 W m^{-1} K^{-1}) is only about one third of the value of the carbon foam (1.745 W m^{-1} K^{-1}). In addition, the thermal conductivity of CF/CA studied by J. Feng is 0.328 W m^{-1} K^{-1} at 300 °C in air.[45] The CF/CA can be used as a promising high-temperature thermal insulator (in inert atmospheres or vacuum) in thermal protection system.

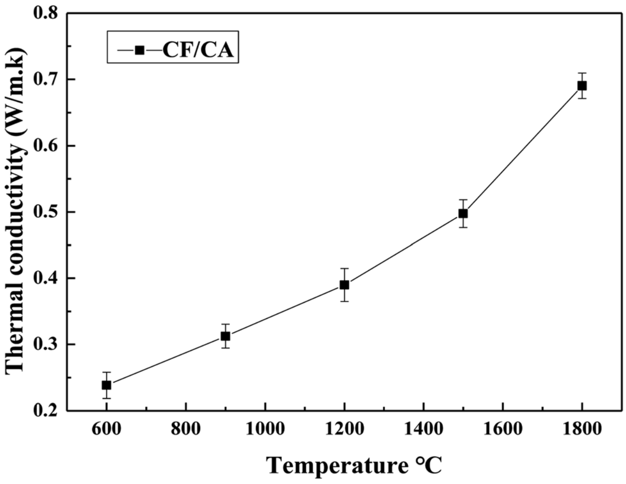

Fig. 14 Thermal conductivities of the CF/CA under various temperature in argon. The error bars indicate the standard error of twenty results of five measure temperatures, with four flash pulses for each measurement temperature.

4. Conclusions

In this study, we developed a novel preparation strategy of CF/CAs *via* combining RF gel containing salt with PAN fiber felts. Compared with the traditional sol–gel method for preparing CF/CAs, this procedure eliminates the need for solvent-exchange and supercritical-fluid drying processes. The obtained CF/CA exhibits low thermal conductivity (0.6904 W m^{-1} K^{-1}) even at temperature as high as 1800 °C under argon atmosphere, and possess relatively high compressive strength (6.10 MPa, 10% ε) and a low density of 0.68 g cm^{-3}. Thus, the CF/CAs can be used as promising candidates for ultrahigh temperature thermal insulation (under inert atmospheres or vacuum) in thermal protection systems such as space vehicles or industrial high temperature furnaces. Our novel strategy may lead to lower-cost and large scale industrial process for preparing CF/CAs.

Conflicts of interest

There are no conflicts to declare.

Acknowledgements

The authors sincerely acknowledge the financial support from National Natural Science Foundation of China (51702360) and Doctor Special Foundation of Jiangxi Academy of Sciences (2020-YYB-14).

References

1 Y. Hanzawa, H. Hatori, N. Yoshizawa and Y. Yamada, *Carbon*, 2002, **40**, 575–581.
2 J. Zhao, C. Lai, Y. Dai and J. Xie, *Mater. Lett.*, 2007, **61**, 4639–4642.
3 A. Tiwari, A. P. Mishra, S. R. Dhakate, R. Khan and S. K. Shukla, *Mater. Lett.*, 2007, **61**, 4587–4590.
4 S. Budhi, H. S. Kibombo, D. Zhao, A. Gonshorowski and R. T. Koodali, *Mater. Lett.*, 2011, **65**, 2136–2138.
5 X. Lu, O. Nilsson and J. Fricke, *J. Appl. Phys.*, 1993, **73**, 581–584.
6 D. Li and X. Zhu, *Mater. Lett.*, 2011, **65**, 1528–1530.
7 M. Deng, Q. Zhou, A. Du, J. Kasteren and Y. Wang, *Mater. Lett.*, 2009, **63**, 1851–1854.
8 W. Liu, Y. Soneda, M. Kodama, J. Yamashita and H. Hatori, *Mater. Lett.*, 2008, **62**, 2766–2768.
9 F. Wang, G. Jung, A. Su, S. Chan, X. Li and M. Duan, *Mater. Lett.*, 2009, **63**, 952–954.
10 J. Feng, J. Feng, Y. Jiang and C. Zhang, *Mater. Lett.*, 2011, **65**, 3454–3456.
11 Y. Hanzawa, H. Hatori, N. Yoshizawa and Y. Yamada, *Carbon*, 2002, **40**, 575–581.

12 J. Feng, J. Feng and C. Zhang, *J. Sol-Gel Sci. Technol.*, 2011, **59**, 371–380.
13 M. Wiener, G. Reichenauer, S. Braxmeier, F. Hemberger and H. P Ebert, *Int. J. Thermophys.*, 2009, **30**, 1372–1385.
14 J. Feng, J. Feng and C. Zhang, *J. Porous Mater.*, 2012, **19**, 551–556.
15 J. Feng, C. Zhang and J. Feng, *Mater. Lett.*, 2012, **67**, 266–268.
16 Y. Shao, C. Guizania, P. Grosseaub, D. Chaussy and D. Beneventi, *Composites, Part B*, 2018, **149**, 206–215.
17 M. Wang, S. Zhang, Z. Zhou, J. Zhu, J. Gao, K. Dai, D. Huang and Z. Li, *Composites, Part B*, 2021, **224**, 109175.
18 D. Pan, Q. Li, W. Zhang, J. Dong, F. Su, V. Murugadoss, Y. Liu, C. Liu, N. Naik and Z. Guo, *Composites, Part B*, 2021, **209**, 108609.
19 D. Pan, Q. Li, W. Zhang, J. Dong, F. Su, V. Murugadoss, Y. Liu, C. Liu, N. Naik and Z. Guo, *Composites, Part B*, 2021, **209**, 108609.
20 Y. Chang, M. Antonietti and T. Fellinger, *Angew. Chem., Int. Ed.*, 2015, **54**, 5507–5512.
21 S. Zhang, J. Feng, J. Feng, Y. Jiang and F. Ding, *Appl. Surf. Sci.*, 2018, **440**, 873–879.
22 M. Yu, J. Li and L. Wang, *Chem. Eng. J.*, 2017, **310**, 300–306.
23 M. Yu, Y. Han, J. Li and L. Wang, *Int. J. Biol. Macromol.*, 2018, **115**, 185–193.
24 K. Li, D. Tang, W. Zhang, Z. Qiao, Y. Liu, Q. Huo, D. Liang, J. Zhu and Z. Zhao, *Mater. Lett.*, 2017, **209**, 256–259.
25 L. Liu, C. Jia, J. He, F. Zhao, D. Fan and L. Xing, *Compos. Sci. Technol.*, 2015, **121**, 56–72.
26 H. Y. Tian, C. E Buckley, M. Paskevicius and S. B Wang, *J. Supercrit. Fluids*, 2011, **55**, 1115–1117.
27 K. Li, D. Tang, W. Zhang, Z. Qiao, Y. Liu, Q. Huo, D. Liang, J. Zhu and Z. Zhao, *Mater. Lett.*, 2017, **209**, 256–259.
28 N. Fechler, S. Wohlgemuth, P. Jaker and M. Antonietti, *J. Mater. Chem. A*, 2013, **1**, 9418–9421.
29 N. Fechler, T. Fellinger and M. Antonietti, *Adv. Mater.*, 2013, **25**, 75–79.
30 G. Wu, J. Yang, D. Wang, R. Xu, K. Amine and C. Lu, *Mater. Lett.*, 2014, **115**, 1–4.
31 Z. Yu, G. Li, N. Fechler, N. Yang, Z. Ma, X. Wang, M. Antonietti and S. Yu, *Angew. Chem., Int. Ed.*, 2016, **55**, 14623–14627.
32 H. Zhang, J. Feng, L. Li, Y. Jiang and J. Feng, *Monatsh. Chem.*, 2018, **149**, 2137–2144.
33 X. Liu, N. Fechler and M. Antonietti, *Chem. Soc. Rev.*, 2013, **42**, 8237–8265.
34 X. Liu and M. Antonietti, *Carbon*, 2014, **69**, 460–466.
35 P. Strubela, H. Althuesa and S. Kaskel, *Carbon*, 2016, **107**, 705–710.
36 H. Guan, Q. Wang, X. Wu, J. Pang, Z. Jiang, G. Chen, C. Dong, L. Wang and C. Gong, *Composites, Part B*, 2021, **207**, 108562.
37 H. Zhang, J. Feng, L. Li, Y. Jiang and J. Feng, *RSC Adv.*, 2019, **9**, 5967–5977.
38 J. Xu, L. Shi, J. Wang, S. Lu, Y. Wang, G. Gao and S. Ding, *Carbon*, 2018, **138**, 348–356.
39 B. Nagy, I. Bakos, I. Bertoti, A. Doman, A. Menyhard, M. Mohai and K. Laszlo, *Carbon*, 2018, **139**, 872–879.
40 P. Xie, W. Sun, Y. Liu, A. Du, Z. Zhang, G. Wu and R. Fan, *Carbon*, 2018, **129**, 598–606.
41 J. Feng, J. Feng, Y. Jiang and C. Zhang, *Mater. Lett.*, 2011, **65**, 3454–3456.
42 C. Moreno-Castilla and F. J. Maldonado-Hódar, *Carbon*, 2005, **43**, 455–465.
43 S. Song, H. Ai, W. Zhu, L. Lv, R. Feng and L. Dong, *Composites, Part B*, 2021, **226**, 109330.
44 A. Vinu, C. Streb, V. Murugesan and M. Hartmann, *J. Phys. Chem. B*, 2003, **107**, 8297–8299.
45 J. Feng, C. Zhang, J. Feng, Y. Jiang and N. Zhao, *ACS Appl. Mater. Interfaces*, 2011, **12**, 4796–4803.
46 M. Wiener, G. Reichenauer, S. Braxmeier, F. Hemberger and H. Ebert, *Int. J. Thermophys.*, 2009, **30**, 1372–1385.
47 D. Zhao, C. Zhang, H. Hu and Y. Zhang, *Ceram. Int.*, 2011, **37**, 2089–2093.